Sensors & Actuators: B. Chemical 376 (2023) 132983

Contents lists available at ScienceDirect

Sensors and Actuators: B. Chemical

journal homepage: www.elsevier.com/locate/snb

Effect of {010} crystal facets of Bi_2MoO_6 and 1D/2D heterostructures for conductometric room temperature NH_3 gas sensors

Kaidi Wu [a,b], Hongfeng Chai [a], Kaichun Xu [a], Marc Debliquy [b], Chao Zhang [a,*]

[a] College of Mechanical Engineering, Yangzhou University, Yangzhou 225127, PR China
[b] Service de Science des Matériaux, Faculté Polytechnique, Université de Mons, Mons 7000, Belgium

ARTICLE INFO

Keywords:
$MWCNTs/Bi_2MoO_6$
Gas sensors
Ammonia
1D/2D heterojunction
Re-orientated crystal facets

ABSTRACT

High working temperature and the insufficient limits of detection limit the broad applications of semiconductor chemiresistive gas sensors. Herein, pure Bi_2MoO_6 nanosheets and a series of one-dimensional/two-dimensional (1D/2D) multi-walled $CNTs/Bi_2MoO_6$ nanocomposites were developed via a facile hydrothermal route for room-temperature ammonia monitoring. The as-synthesized samples were characterized by various analytical techniques. 0.5 wt% $MWCNTs/Bi_2MoO_6$ nanocomposites showed the best sensing properties to 10–50 ppm NH_3, including low limit of detection (157 ppb), high response (R_a/R_g = 44.2 @ 50 ppm), good selectivity, reproductivity, and anti-humidity sensing ability. The enhanced gas sensing mechanism was proposed based on the synergetic effect of high-energy crystal facets, modified surface characteristics and p-n heterojunction. Density functional theory (DFT) studies were also carried out to further clarify the gas sensing mechanisms. This work provides a practical approach to design and fabricate high-precision gas sensors working at room temperature.

1. Introduction

As an indicator of assessing the environmental and indoor pollutants level, NH_3 will also damage the human health once its concentration exceeds 50 ppm for 8 h [1,2]. NH_3 is also an indexed gas for protein-rich food quality assessment, which will be released with the concentration of ppm level during food spoilage process [3,4]. Moreover, the change of NH_3 concentration from human exhaled breath can be used to diagnose some diseases about the liver and lung [5]. Hence, real-time detecting NH_3 is significant for ensuring the environmental quality and human health, which can be realized through the high-performance NH_3 gas sensors [6].

Various metal oxide semiconductor-based chemiresistive NH_3 sensors have been designed in the past few years, such as ZnO, SnO_2, WO_3, In_2O_3, TiO_2, Co_3O_4 and $CuFe_2O_4$ [7–13]. To attain better sensing properties, multiple strengthening methods have been utilized to improve the electronic or surface characteristics, such as fabricating porous or hierarchical nanostructures, doping with noble metals or transition metal elements, and introducing homo/hetero-junctions [14,15]. However, the challenge of high working temperature and insufficient detection range remains, leading to poor operating stability of gas sensors and limited practical application potential [16].

Bismuth molybdate (Bi_2MoO_6), as a kind of Aurivillius oxide with octahedral $[MoO_4]^{2-}$ perovskite layer and $[Bi_2O_2]^{2+}$ layers, has been investigated as photocatalysts because of that the alternating layered structure and the corresponding in-built electric field between the layers can improve the electron mobility and reaction kinetics at the interface [17–20]. However, the application of Bi_2MoO_6 in gas sensors is rarely reported, especially for room temperature NH_3 detection. Qin et al. studied the NH_3 sensing performance of flower-like Bi_2MoO_6, and the sensor displayed a fine response to NH_3 at 75 °C [21]. Hence, the tunable bimetallic oxide Bi_2MoO_6 with a narrow bandgap of 2.5–2.7 eV should be a candidate for low or room-temperature NH_3 detection.

Additionally, multi-walled carbon nanotubes (MWCNTs) are reported as NH_3 sensing materials with room-temperature operation mode and satisfactory selectivity. Bannov et al. developed a series of NH_3 sensors based on oxygen plasma treated MWCNTs, which showed a fine response to 10–500 ppm NH_3 at room temperature [22]. Panes-Ruiz et al. reported that the semiconducting CNTs showed fine response towards NH_3 (5% @ 10 ppm) [23]. Yang et al. prepared the $NiWO_4$/MWCNTs gas sensor with p-n heterojunction, showing enhanced response and selectivity to 20–80 ppm NH_3 [24]. These studies prove that introducing MWCNT has many advantages in the electrical system, such as enhanced surface activity and accelerated carrier transport.

* Correspondence to: College of Mechanical Engineering, Yangzhou University, Huayang West Road 196, Yangzhou 225127, Jiangsu Province, PR China.
E-mail address: zhangc@yzu.edu.cn (C. Zhang).

https://doi.org/10.1016/j.snb.2022.132983
Received 8 June 2022; Received in revised form 3 November 2022; Accepted 9 November 2022
Available online 12 November 2022

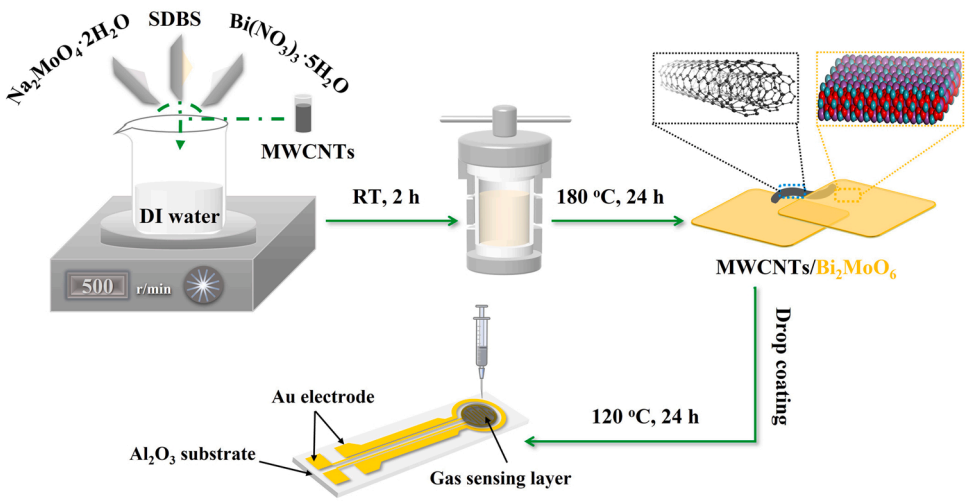

Scheme 1. Fabrication procedures of Bi_2MoO_6 nanosheets and MWCNTs/Bi_2MoO_6 gas sensors.

To our best knowledge, there is no reported work about pure Bi_2MoO_6 and its composites for room temperature gas sensors. Motivated by the concepts mentioned above, we developed 2D Bi_2MoO_6 nanosheets and 1D/2D MWCNTs/Bi_2MoO_6 nanocomposites based NH_3 sensors using the hydrothermal method and drop coating. The effect of MWCNTs on composites was systematically studied, and the NH_3 sensors were also evaluated at room temperature. The enhanced sensing mechanisms were revealed based on the surface conduction model and DFT calculations.

2. Experimental section

2.1. Synthesis of Bi_2MoO_6 nanosheets and MWCNTs/Bi_2MoO_6 composites

The MWCNTs suspension (2 mg/mL) was first prepared as follows:

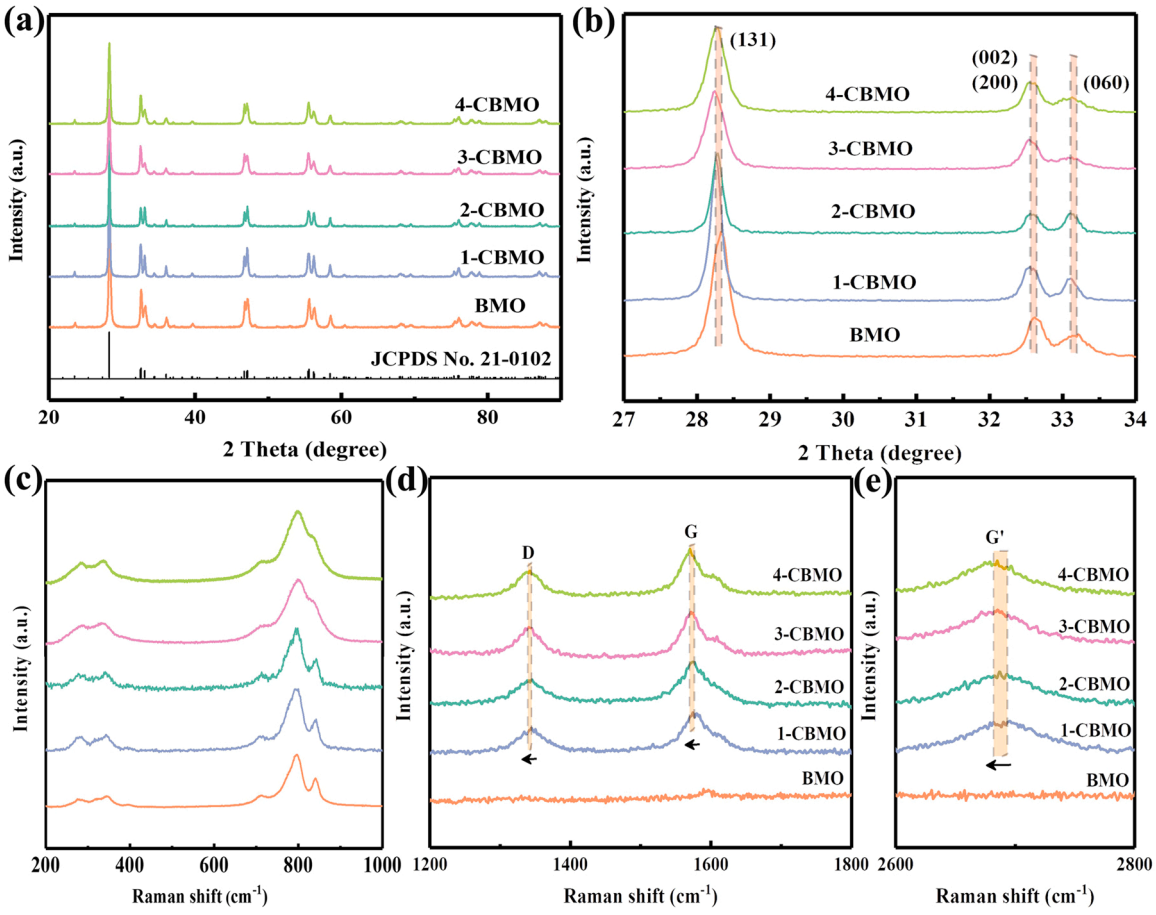

Fig. 1. XRD patterns of pure Bi_2MoO_6 nanosheets and MWCNTs/Bi_2MoO_6 composites in (a) 20–90° and (b) 27–34°; (c-e) Raman spectra of pure Bi_2MoO_6 nanosheets and MWCNTs/Bi_2MoO_6 composites.

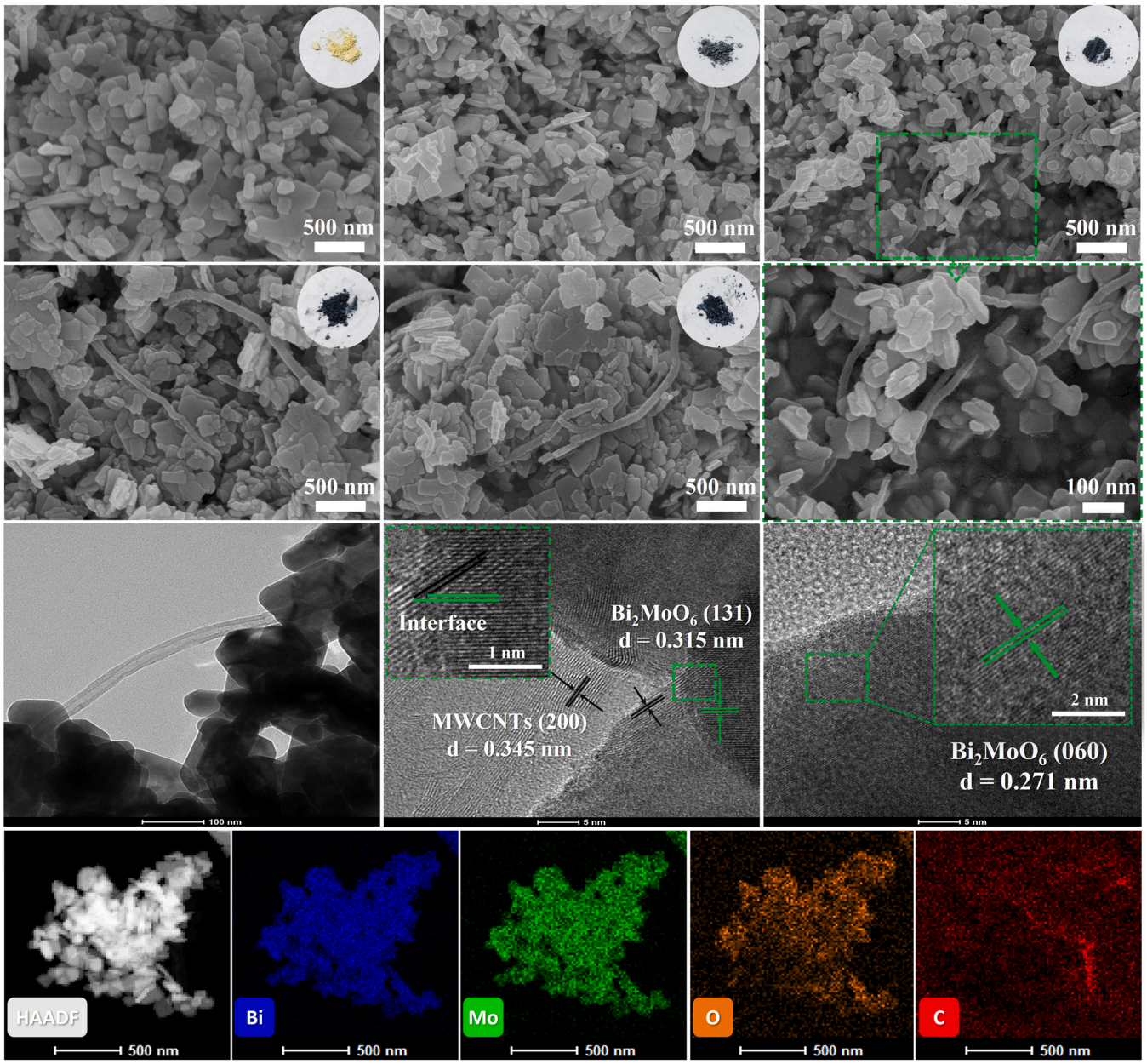

Fig. 2. FESEM images of (a) pure BMO nanosheets, (b-e) CBMO composites and (f) high-resolution image of the selected region of 2-CBMO, nanostructured details of 2-CBMO composite: (g) HR-TEM images, (h, i) lattice distance of various crystal planes and (j-n) HAADF image and EDS elements mappings of 2-CBMO.

30 mg MWCNTs (Nanjing XFNANO Materials Technology Co., Ltd) was added into 15 mL N,N-Dimethylformamide (DMF). The target solution can be obtained after ultrasonication for 2 h.

All other chemical reagents (Shanghai Aladdin Biochemical Technology Co., Ltd.) were used without further purification. Bi_2MoO_6 nanosheets and MWCNTs/Bi_2MoO_6 composites were synthesized as illustrated in Scheme 1. The typical hydrothermal procedure is that 0.97 g $Bi(NO_3)_30.5\ H_2O$, 0.242 g $Na_2MoO_40.2\ H_2O$, and 0.0366 g Sodium dodecyl benzene sulphonate were mixed in 30 mL deionized water. MWCNTs solution was dropped into the mixed solution. The final solution was transferred into a Teflon-lined stainless autoclave (50 mL) after magnetically stirred for 2 h, which was subsequently kept at 180 °C for 24 h. After cooling down naturally, the powders were washed with deionized water and absolute ethanol for 5 times. The as-synthesized products were obtained after being dried at 80 °C for 15 h. These samples compounded with MWCNTs of 0, 1.125 mL, 2.25 mL, 3.375 mL, and 4.50 mL are denoted as Bi_2MoO_6 (BMO), 0.25 wt% MWCNTs/Bi_2MoO_6 (1-CBMO), 0.5 wt% MWCNTs/Bi_2MoO_6 (2-CBMO), 0.75 wt% MWCNTs/Bi_2MoO_6 (3-CBMO) and 1 wt% MWCNTs/Bi_2MoO_6 (4-CBMO).

2.2. Characterization

The phase structure of five powders was investigated by X-ray diffraction using Cu-Kα radiation (XRD, D8 Advance Bruker, λ = 1.54182 Å) and micro-Raman spectroscopy (MRS, In via, Renishaw). The morphological characteristics and nanostructure details were determined via field-emission scanning electron microscopy (FESEM, S4800II Hitachi), transmission electron microscopy (TEM, JEM-2100) and high-resolution transmission electron microscopy (HRTEM, Tecnai G2 F30 S-TWIN). The surface elements states were analyzed using X-ray photoelectron spectroscopy (XPS, Thermo Fisher Scientific ESCALAB 250Xi). The specific surface areas (BET) were calculated using N_2 adsorption/desorption isotherms (Autosorb IQ3, Quantachrome Instruments). Ultraviolet-visual-Near-Infrared (Uv-vis)

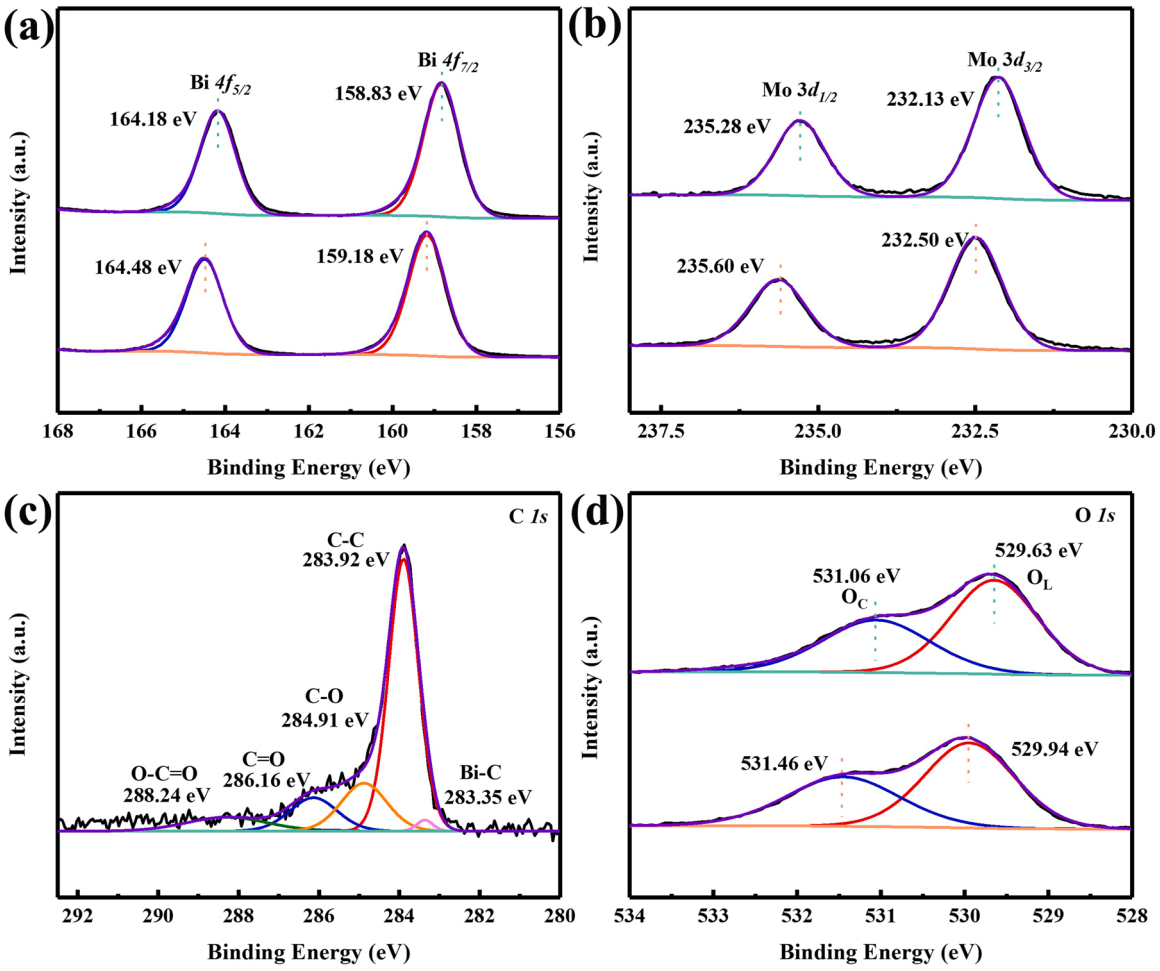

Fig. 3. Elements chemical states of pure BMO and 2-CBMO determined via XPS: (a) Bi *4 f* and (b) Mo *3d* of BMO and 2-CBMO, (c) C *1 s* of 2-CBMO and (d) O *1 s* of BMO and 2-CBMO.

spectrometer (Cary 5000) was used to measure Uv-vis spectral absorption and calculate energy band gap. Ultraviolet photoelectron spectroscopy (UPS) was performed to determine the work function in the same instrument with unmonochromatized He I radiation.

2.3. Fabrication and measurement of gas sensors

The target suspensions were obtained by mixing as-synthesized powders with deionized water, then drop coating onto the Al_2O_3 substrate equipped with interdigital Au electrodes (Scheme 1). These gas sensors were obtained after being aged at 120 °C for 24 h. The room temperature (25 ± 1 °C) gas sensors testing system is displayed in Fig. S1, and the relative humidity of Lab is 30 ± 10%RH. More testing details have been added in Supplement materials. The response (n-type) is calculated using R_a/R_g (R_a and R_g represent the stable resistance values in air and target gas, respectively). The response/recovery time is the time required to reach a 90% change of resistance in a full sensing behavior.

2.4. DFT calculation

The adsorption behaviors between sensing material surface and target gas were simulated by the CASTEP modules (Material Studio). The configuration parameters were added in Supplement materials. The adsorption energy of target gases molecules on Bi_2MoO_6 or MWCNTs/Bi_2MoO_6 was expressed as Eq. (1):

$$E_{ads} = E_{total} - (E_{facets} + E_{ammonia}) \quad (1)$$

where E_{total} represents the total energy of ammonia molecule - certain crystal facet of Bi_2MoO_6 surface system, E_{facets} is the energy of (002) or (060) Bi_2MoO_6, and $E_{ammonia}$ represents the energy of the isolated ammonia molecule.

3. Results and discussion

3.1. Structural and morphological characteristics

The phase structure of pure Bi_2MoO_6 and MWCNTs/Bi_2MoO_6 nanocomposites are shown in Fig. 1a. The characteristics peaks from 20° to 90° were indexed to the standard diffraction patterns of orthorhombic Bi_2MoO_6 (JCPDS 21–0102). Due to the compounding contents of MWCNTs being too low, no significant characteristic peaks could be observed in all MWCNTs/Bi_2MoO_6 powders [25]. The enlarged patterns from 27° to 34° in Fig. 1b show that the characteristic peaks of these composites became weaken and broadened with the increased MWCNTs content, suggesting a gradual decrease in the crystallization degree, which was in good accordance with the previous studies [26,27]. Additionally, the peaks of nanocomposites at $2\theta = 28.3°$, 32.6° and 33.2° gradually shift to the low angle direction, and the diffraction intensity decrease, which further confirms the increase of MWCNTs content [28]. Moreover, it is noteworthy that there are significant differences in the relative intensities of (131), (200)/(002), and (060) planes, indicating the possibility of different preferential orientation growth under different MWCNTs mass fractions. Especially, the

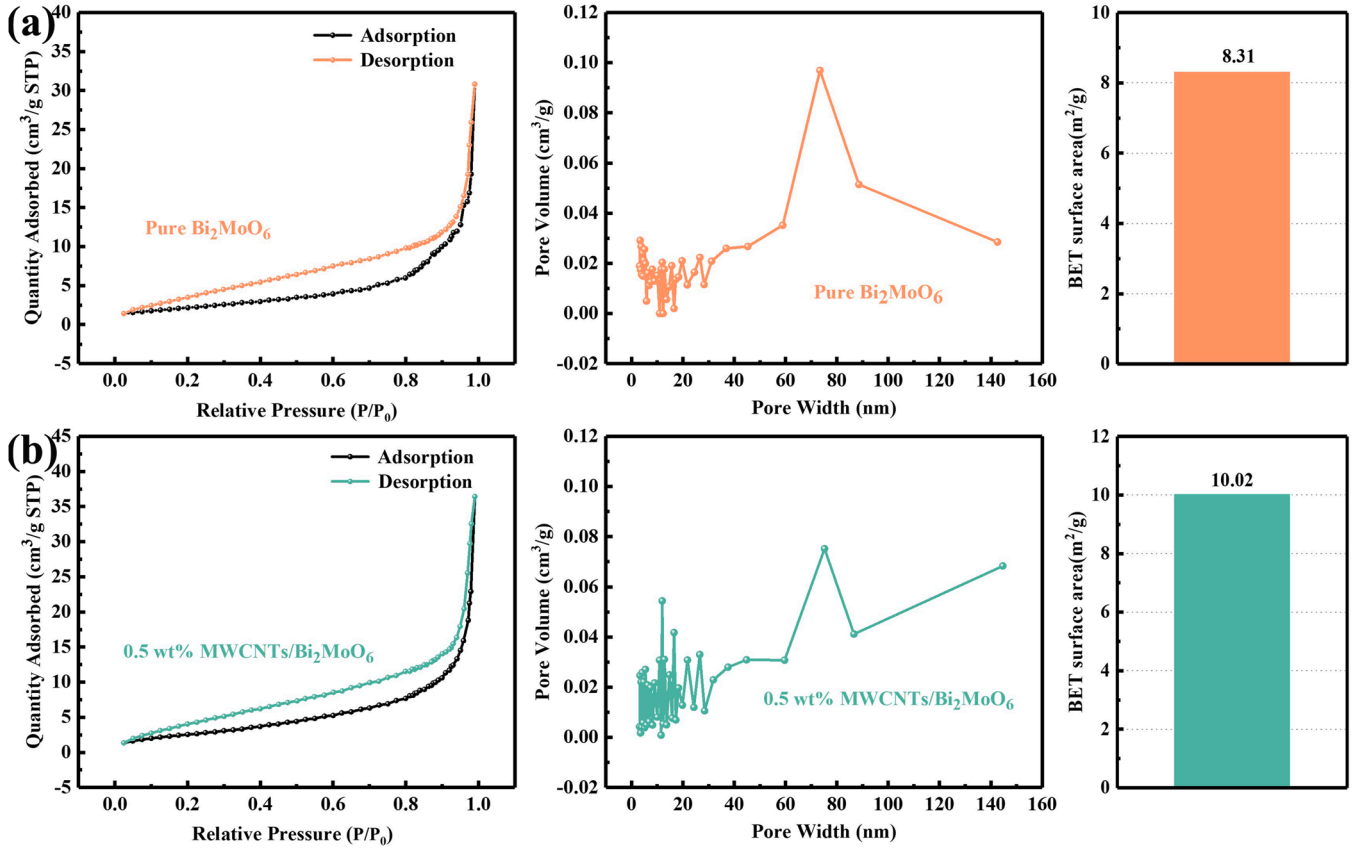

Fig. 4. N_2 adsorption-desorption isotherms, pore size distribution and BET specific surface areas of (a) BMO and (b) 2-CBMO composites.

intensity ratios of (060) and (200)/(002) planes of 2-CBMO increased significantly, indicating that the part of crystals would grow along the {010} direction and form rod-like nanostructure rather than {001} square-sheet nanostructure [29,30]. The analysis will be further proved by the SEM and TEM inspection. The re-orientated growth effect of MWCNTs on the exposed facets of {010} with higher surface energies will be further discussed in gas sensing mechanisms [19].

Raman spectra were carried out to further identify the composition of all samples. In Fig. 1c, all the samples show similar stretching vibrations at 200–1000 cm^{-1}. The peaks at 200–400 cm^{-1} are ascribed to the MoO_4 octahedra and Bi_2O_2 tetrahedra [30]. The peaks in 650–900 cm^{-1} are ascribed to the bending motions and stretching vibrations of MoO_4 octahedra, confirming the formation of Bi_2MoO_6 in all samples [17]. The peaks of Bi_2MoO_6 at 800 cm^{-1} shift to a lower wavenumber, indicating the synergistic interaction between MWCNTs and Bi_2MoO_6. In Fig. 1d, two peaks at around 1351 cm^{-1} and 1577 cm^{-1} are corresponded to the characteristic D (disordered sp^2 and non-sp^2 carbon defects) and G (the C-C vibration with the sp^2 hybridized orbital) bands of CNTs [31]. Notably, the peaks of D and G-bands present a slight blue shift, indicating a large number of disordered structures in the composites and the accelerated electron transfer between MWCNTs and Bi_2MoO_6 [32]. Fig. 1e shows the 2D bands of the MWCNTs at around 2675 cm^{-1}, associated with the splitting of electron bands [31]. Therefore, the results confirm the successful introduction of MWCNTs and the compounding between MWCNTs and Bi_2MoO_6.

The morphology of all samples was characterized using FESEM. In Fig. 2a, pure Bi_2MoO_6 showed nanosheet structure with a thickness of around 5 nm. In Fig. 2b and c, the composite samples with 0.25 and 0.5 wt% MWCNTs showed uniformly distributed microstructure, which consist of Bi_2MoO_6 nanosheets and carbon nanotubes. With increased MWCNTs content, the samples with 0.75 and 1 wt% MWCNTs showed nanosheet-stacked structure and a part of larger-scale sheets (Fig. 2d and e,). Fig. S2 provides more surface morphology characteristics of all five samples, which can further confirm the above FESEM analysis. Moreover, the surface morphology of the as-fabricated BMO and 2-CBMO sensors was also observed. As shown in Fig. S3, the surface morphology of BMO and 2-CBMO sensors are similar to that of the as-synthesized powders, showing the uniformly distributed nanosheets structure of BMO (Fig. S3a and b) and sheets-like Bi_2MoO_6 and carbon nanotubes of 2-CBMO sensors (Fig. S3c and d). The nanostructure of MWCNTs, pure BMO and 2-CBMO was analyzed via TEM and HRTEM. In Fig. S4, the pristine MWCNTs with a diameter of about 23.4 nm are observed and present a lattice distance of around 0.35 nm, which was attributed to the (002) [33]. As shown in Fig. S5, BMO presents various scaled nanosheets, while 2-CBMO shows MWCNTs interacted with smaller BMO nanosheets and nanorods. Fig. S6 shows the HRTEM images of BMO, the lattice distance was measured as 0.275 nm, which was attributed to (200), and the synthesized BMO displayed a uniform elements distribution of Bi, Mo, and O. The HRTEM images of 2-CBMO in Fig. 2g clearly show that MWCNTs are well compounded with Bi_2MoO_6. An interface with closely contacted MWCNTs and Bi_2MoO_6 was observed in Fig. 2h. The interplanar lattice distances of 0.345 nm and 0.315 nm are indexed to (200) of MWCNTs and (131) of Bi_2MoO_6 nanosheets, respectively [19]. In Fig. 2i, the interplanar lattice distance of 0.271 nm is indexed to (060) planes of Bi_2MoO_6 [34], which confirms the results of XRD analysis. The SAED patterns in Fig. S7 show the Debye-Scherrer rings for the crystal planes of Bi_2MoO_6 and MWCNTs, confirming the excellent polycrystal quality of 2-CBMO composite. Furthermore, the homogeneous elemental distribution of C, Bi, Mo, and O in 2-CBMO composite is demonstrated in Fig. 2j-n.

The elemental compositions and their oxidation states of BMO and 2-CBMO were analyzed using XPS. The full survey spectrum of the two samples in Fig. S8 shows the presence of Bi, Mo, and O elements in the two powders. And the obvious C peak from MWCNTs can be found in 2-

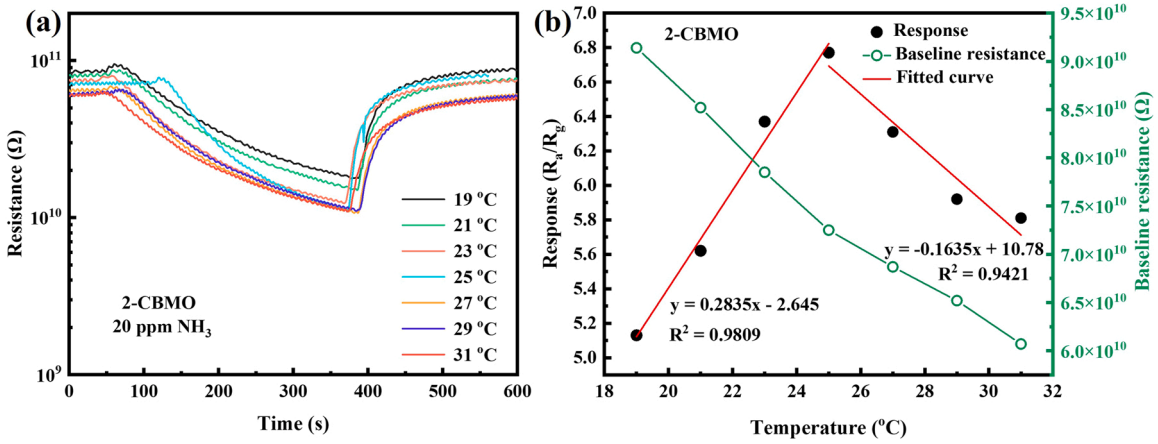

Fig. 5. The effect of working temperature (around room temperature) on the response and baseline resistance of 2-CBMO.

CBMO. As shown in Fig. 3a, the two peaks at binding energies of 159.18 and 164.48 eV in BMO spectra are assigned to Bi 4f7/2 and Bi 4f5/2, respectively [35]. Additionally, the two similar peaks are also observed in 2-CBMO, demonstrating the presentence of Bi^{3+} in both powders. The Mo 3d spectra (Fig. 3b) are fitted with two peaks of Mo 3d1/2 at around 235 eV and Mo 3d3/2 at around 232 eV, indicating the existence of Mo^{6+} in both samples [35]. Significantly, the main peaks of Bi 4 f and Mo 3d of 2-CBMO show a slight shift to the lower binding energy, which may be ascribed to the electron transfer between Bi_2MoO_6 with MWCNTs and the effect of MWCNTs on the chemical environment of Bi^{3+} and Mo^{6+} [36]. The high-resolution C 1 s XPS spectrum of 2-CBMO in Fig. 3c contained five peaks at 283.92 (C-C), 284.91 (C-O), 286.16 (C═O), 288.24 (O-C═O), and 283.35 eV (Bi-C), indicating that the MWCNTs were compounded with Bi_2MoO_6 by Bi-C covalent bonds [37, 38]. The O 1 s spectra in Fig. 3d can be fitted with two peaks at 529.94 eV and 531.46 eV, regarding to the lattice oxygen, and surface chemisorbed oxygen, respectively. As for 2-CBMO, the two main peaks are located at the lower binding energy of 529.63, and 531.06 eV, respectively [39]. The shift to the lower binding energy of O 1 s peaks is attributed to the formation of p-MWCNTs/n-Bi_2MoO_6 heterojunction, which can improve the electron density around oxygen atoms [40].

The BET specific surface area (S_{BET}) and pores distribution of pure BMO nanosheets and 2-CBMO composites were analyzed. Fig. 4 shows the isotherm plots of BMO and 2-CBMO. The calculated S_{BET} of BMO and 2-CBMO were 8.31 and 10.02 $m^2 \cdot g^{-1}$, respectively. The mean pore sizes of BMO and 2-CBMO were 3.307 and 3.306 nm, respectively (Table S1). Moreover, 2-CBMO also presented a larger total pore volumes (0.056 $cm^3 \cdot g^{-1}$), while pure BMO was 0.047 $cm^3 \cdot g^{-1}$ (Table S1). Hence,

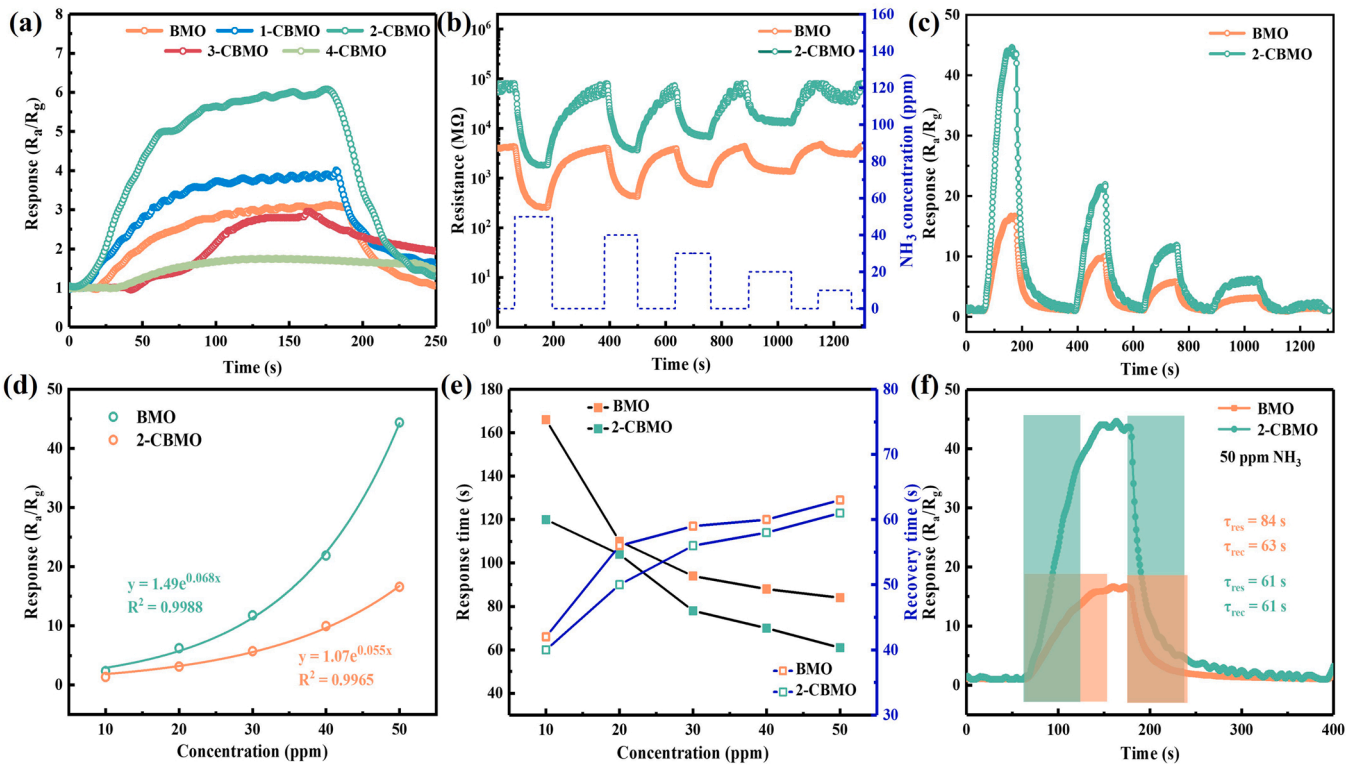

Fig. 6. (a) response values of pure BMO and CBMO composites to 20 ppm NH_3 at room temperature. (b) dynamic response/recovery curves of five samples to 10–50 ppm NH_3 at room temperature. (c) responses values of BMO and 2-CBMO to 10–50 ppm NH_3 at room temperature. (d) relationship of response values versus NH_3 concentration. (e) responses/recovery time of BMO and 2-CBMO to 10–50 ppm NH_3 at room temperature. (f) responses/recovery time of BMO and 2-CBMO to 50 ppm NH_3 at room temperature.

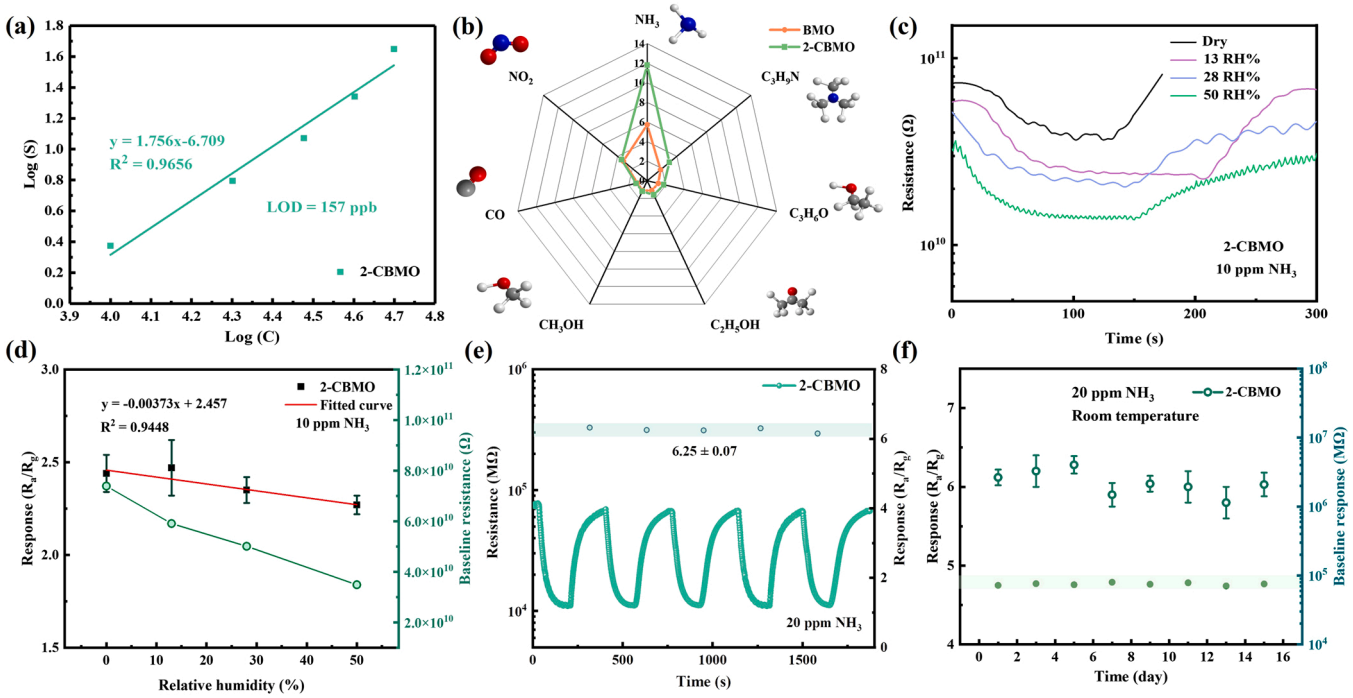

Fig. 7. (a) Relationship of logarithmic response values versus NH_3 concentration. (b) Selectivity to 20 ppm NH_3 and other interfering gases of BMO and 2-CBMO at RT. (c) The dynamic resistance curves of 2-CBMO to 10 ppm NH_3 under relative humidity of 0–50%. (d) The variation of baseline resistance and response values of 2-CBMO versus relative humidity. (e) response to 20 ppm NH_3 of 2-CBMO in 5 cycles. (f) baseline resistance and response stable characteristics of 2-CBMO sensor to 20 ppm NH_3 in 15 days.

the improved surface characteristics of 2-CBMO will favor attaining superior sensing properties, resulting from the boosted adsorption and diffusion of gas molecules.

3.2. Gas sensing performance

The sensing response of 0.5 wt% MWCNTs/Bi_2MoO_6 gas sensor to 20 ppm NH_3 at around room temperatures (25 ± 6 °C) were investigated. As shown in Fig. 5, it can be seen that the sensing response of the 0.5 wt% MWCNTs/Bi_2MoO_6 sensor varied linearly from 5.13 to 6.77 when the working temperature increased from 19 °C to 25 °C (Slope = 0.2835, R^2 = 0.9809). When the working temperature increased from 25 to 31 °C, the sensor response values varied from 6.77 to 5.81 (Slope = −0.1635, R^2 = 0.9421). The linear response of 2-CBMO (Slope = 0.4715, R^2 = 0.9788) to 10–30 ppm NH_3 was also obtained (Fig. S9). Hence, the slope values were used to calculate the effect of working temperature variations on the response. As we calculated, 1 °C temperature increase (decrease) around 25 °C has the same effect on the sensor response than 601.2 ppb (346.7 ppb) NH_3 concentration change.

Fig. S10 displays the dynamic resistance of all gas sensors upon exposure to 20 ppm NH_3 at room temperature (25 ± 1 °C), in which the response value of 2-CBMO gas sensor is significantly higher than that of pure BMO nanosheets and the other CBMO composites (Fig. 6a). Fig. S10b shows the baseline resistance (R_a) values of all gas sensors, the increased change from 4.23×10^9 to 7.66×10^{10} Ω in R_a induced by compounding with MWCNTs of 0.25 wt% and 0.5 wt% could be dominantly attributed to the formation of p-n heterojunctions, and the declined change from 7.66×10^{10} to 2.66×10^9 Ω in R_a induced by compounding with more MWCNTs of 0.75 wt% and 1 wt% could be dominantly attributed to the high conductivity of MWCNTs. Fig. 6b and c show the dynamic resistance and the corresponding response values of BMO and 2-CBMO gas sensors towards 10–50 ppm NH_3. the response values of 2-CBMO to 10–50 ppm NH_3 are 2.37–44.40, while that of pure BMO to 10–50 ppm NH_3 is only 1.37–16.75. In Fig. 6d, the fitted curves show that BMO and 2-CBMO gas sensors possessed exponential relationships (R^2 =0.9965 and R^2 =0.9988) with NH_3 concentrations from 10 to 50 ppm. Moreover, the response/recovery speeds of BMO and 2-CBMO to 10–50 ppm NH_3 were also analyzed. As shown in Fig. 6e, the 2-CBMO gas sensor displayed shorter times in both response and recovery, which could be attributed to MWCNTs compounding and the p-n heterojunction. In detail, Fig. 6 f shows that the 2-CBMO possessed a shorter response/recovery time (61 s/61 s) to 50 ppm NH_3, while BMO was 84 s and 63 s, respectively.

As shown in Figs. 7a, 2-CBMO presents a good linear relationship between the logarithmic concentration with the response values, where the slope (k) is 1.756 and R^2 is 0.9656. The signal-to-noise ratio (RMS_{noise}) of 2-CBMO is calculated as 0.092 based on 50 baseline resistance points from Fig. 6b. Hence, the limit of detection (LOD) of 2-CBMO composite was estimated using LOD = 3 RMS_{noise}/k as 157 ppb [41], which is a satisficed value for practical application.

In Fig. 7b, BMO nanosheets and 2-CBMO composites gas sensors were investigated using C_3H_9N, C_3H_6O, C_2H_5OH, CH_3OH, and CO of 30 ppm and 5 ppm NO_2 under the same test condition. The 2-CBMO shows a significantly higher response of 11.8 to NH_3, indicating 2-CBMO presents enhanced selectivity to NH_3. The effect of relative humidity on 0.5 wt% MWCNTs/Bi_2MoO_6 gas sensor was retested at a RH range from 0% to 50%. Fig. 7c and d show the humidity dependence of response and baseline resistance. The baseline resistances (R_a) were 7.39×10^{10} Ω, 5.91×10^{10} Ω, 5.01×10^{10} Ω and 3.49×10^{10} Ω along with the increasing relative humidity from 0% to 50 RH%, and the corresponding response values to 10 ppm NH_3 were 2.44, 2.47, 2.35 and 2.27, respectively. The response values stay in a stable range, and the variation does not exceed 8%, which is attributed to that the hydrophobic nature of CNTs hinders their sensing ability to humidity [42]. The similar results could be also found in the reported work [43,44]. Though the response values stay in a stable range, there still exist a linear relationship (Slope = −0.00373, R^2 = 0.9448) between material response value and humidity (Fig. 7d). Hence, from this data, 1% RH change only has the same effect on the sensor response than 7.9 ppb NH_3 concentration change. As for reproducibility and stability, we evaluated

Table 1
Ammonia sensing properties of metal oxides-based semiconductor sensors.

Materials	Working Condition	Conc. (ppm)	Response	Humidity resistance[c]	LOD (ppb)	Refs.
ZnO	27 °C	80	2.05[a]	31%	500	[45]
SnO_2	25 °C	300	2.11[a]	30%	500	[46]
CeO_2	25 °C	50	6.65[a]	–	500	[47]
MoO_3	200 °C	50	1.75[a]	–	5000	[48]
$TiO_2/Ti_3C_2T_x$	25 °C	10	1.03[b]	33%	2000	[49]
$NiWO_4$/MWCNTs	460 °C	50	1.82[a]	30%	20,000	[24]
ZnO-MWCNT	25 °C	20	1.02[b]	–	10,000	[50]
2-CBMO	25 °C	50	44.4[a]	8%	157.2	This work

[a] $S = R_a/R_g$, [b] $S = R_g/R_a$, [c] the dropped variation of response values under 0–50 RH%, - not mentioned.

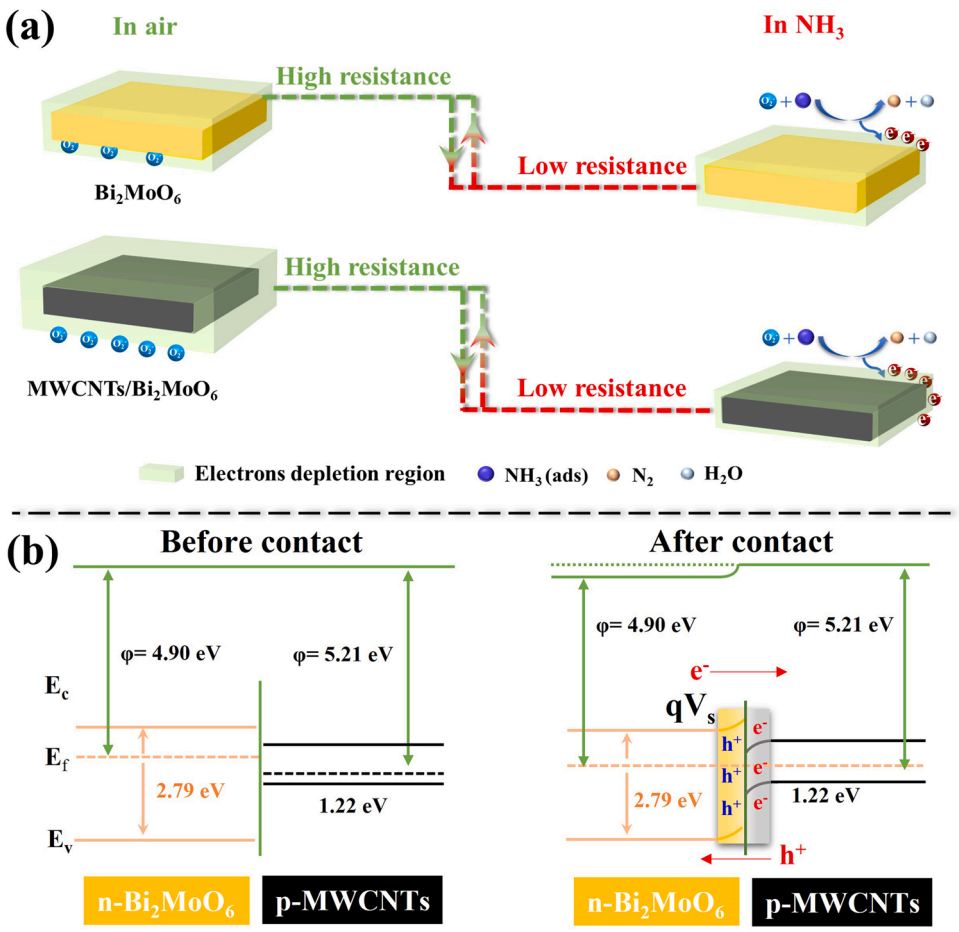

Fig. 8. (a) Adsorption and reaction model of the NH_3 sensing process on the surface of pure BMO nanosheets and 2-CBMO composite-based gas sensor. (b) Energy bands model of the formation of p-n heterojunction structure.

the continuous sensing behavior of 2-CBMO towards 20 ppm NH_3 in five cycles, showing stable response values of around 6.25 (Fig. 7e). Fig. 7f also displayed the stable baseline resistance and response values of 2-CBMO towards 20 ppm NH_3 in 15 days, indicating that 2-CBMO composite attained good operating stability.

The comparison with the NH_3 sensing properties of recently reported metal oxides based gas sensors are shown in Table 1. 2-CBMO composite exhibits superior room- temperature NH_3 sensing properties than the listed gas sensors. The gas sensor in this work will be a competitive candidate in practical application.

3.3. Gas sensing mechanism

Herein, we proposed a possible sensing process. As shown in Fig. 8a, the fabricated Bi_2MoO_6 nanosheets and MWCNTs/Bi_2MoO_6 composites based NH_3 sensors show typical n-type semiconductor behavior during gas sensing tests. Once the sensing materials are exposed to air, oxygen molecules will adsorb and generate chemisorbed oxygen species (O_2^-) on the surface. This process decreases the electrons concentration, forming the electron depletion layer (EDL) at the interface and leading to low conductivity of the sensor. According to the results of the reported work, O_2^- ions could convert NH_3 to N_2 and H_2O at room temperature [51,52]. Therefore, once upon exposure to NH_3, the redox reaction occurred between NH_3 and O_2^- will release the electrons back to the conduction band, resulting in a thinner EDL and a decrease in resistance. The above procedures can be expressed as Eqs. (2)–(5) [51–53]:

$$O_{2\ (gas)} \rightarrow O_{2\ (ads)} \quad (2)$$

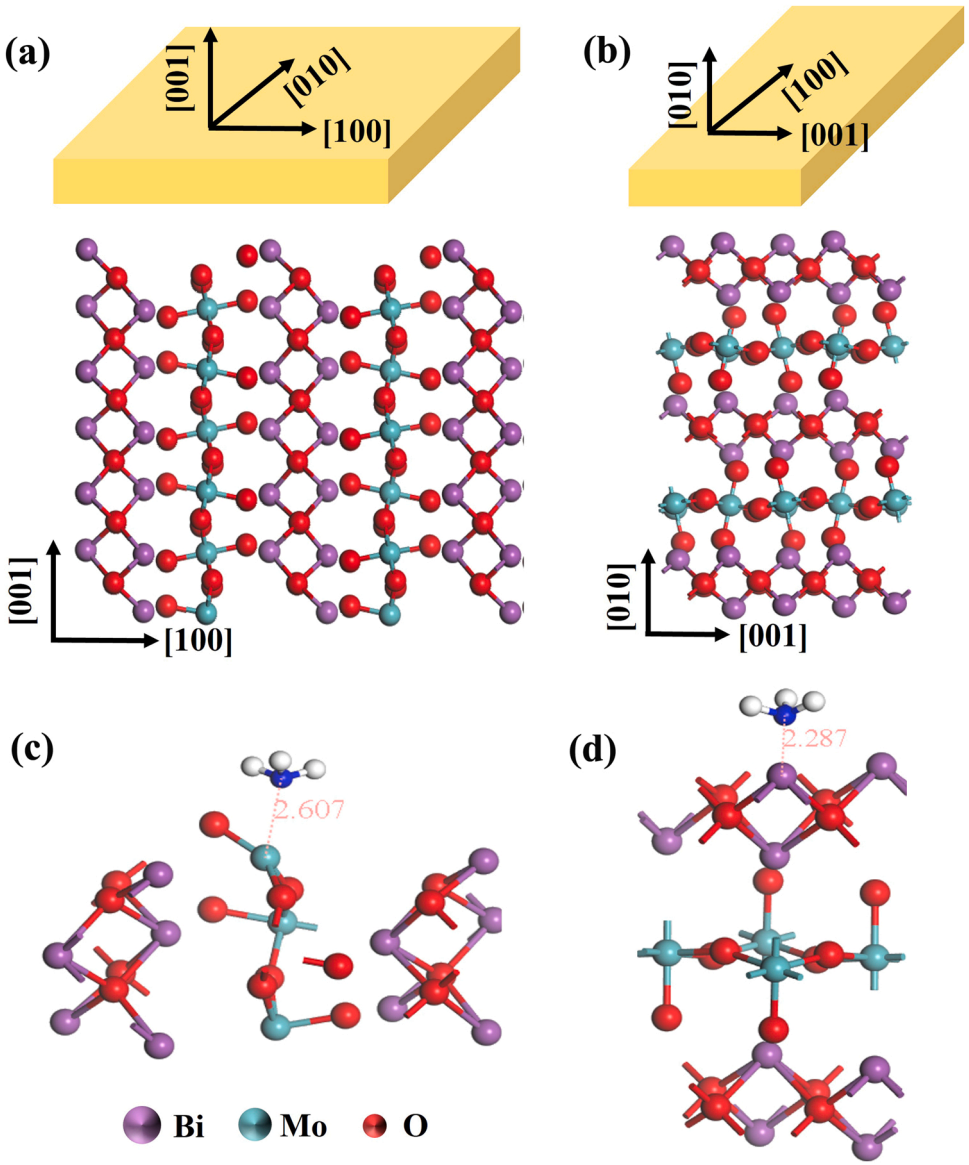

Fig. 9. (a, b) Schematical diagram and geometry structure of {001} and {010} facets. Optimized configurations of NH_3 adsorption on (c) (002) BMO and (d) (060) BMO.

$$O_{2\ (ads)} + e^- \rightarrow O_{2\ (ads)}^- \quad (3)$$

$$NH_{3\ (gas)} \rightarrow NH_{3\ (ads)} \quad (4)$$

$$4NH_{3\ (ads)} + 3\ O_{2\ (ads)}^- \rightarrow 2\ N_2 + 6\ H_2O + 3e^- \quad (5)$$

The enhanced NH_3 sensing mechanisms of 2-CBMO are proposed based on the following factors. Firstly, the synthesized 2-CBMO composites had a larger S_{BET} and total pores volumes than that of pure BMO (Fig. 4 and Table S1), which can facilitate the gas diffusion and provide abundant active sites, thus achieving improved response kinetics and sensing performance [54]. Secondly, as shown in Fig. 3d and Table S2, the estimated atom percentage of surface chemisorbed oxygen species (O_C) for 2-CBMO is 45.1 at%, while BMO is 35.2 at%. The results are also consistent with the first point about BET analysis. Consequently, the abundant O_C species favor forming the thicker depletion layer (lowering the carrier concentration) in air and facilitating the efficient reaction between O_C and NH_3 (increasing the variation of carrier concentration).

Thirdly, in addition to the electronic nature of MWCNTs and Bi_2MoO_6, the formation of p-n MWCNTs/Bi_2MoO_6 heterojunction also plays a key role in the enhanced sensing characteristics of the composites. Uv-vis and UPS spectra were utilized to estimate the exact optical band gap width and work function of as-synthesized Bi_2MoO_6 and MWCNTs samples. The estimated band gap was calculated following the formula $\alpha h\nu = A(h\nu - E_g)^{\eta}$, where α, h, A and E_g refer the reflect coefficient, Planck constant, a constant and bandgap energy, respectively [55]. Herein, $\eta = 2$ owing to the indirect semiconductor properties of Bi_2MoO_6, while $\eta = 1/2$ owing to the direct p-type semiconductor properties of MWCNTs. The calculated band gaps of Bi_2MoO_6 and MWCNTs are 2.79 eV and 1.22 eV, respectively (Fig. S11). The work functions of samples can be calculated by the following equation [56], φ (work function) = $h\nu - (E_{cut-off} - E_{Fermi})$, the energy source in the UPS measurement is He I (hv = 21.22 eV), and $E_{Fermi} = 0$ eV. Therefore, the work functions of Bi_2MoO_6 and MWCNTs were estimated as 4.90 eV and 5.21 eV (Fig. S12a and c). Accordingly, the E_F of Bi_2MoO_6 and MWCNTs were confirmed as - 4.9 eV and − 5.21 eV. Besides, the highest occupied state (HOS) of Bi_2MoO_6 and MWCNTs samples were 2.54 eV and 1.14 eV (Fig. S12 b and d). The corresponding E_V level ($E_V = E_F - E_{HOS}$) obtained from UPS analysis were - 7.44 eV for Bi_2MoO_6 and - 6.35 eV for MWCNTs. In summarize, Table S3 shows the E_F, E_V and E_C of Bi_2MoO_6 were - 4.9 eV, − 7.44 eV and − 4.75 eV, respectively. While those of MWCNTs were - 5.21 eV, − 6.35 eV and − 5.13 eV, respectively. Due to

the difference in work functions, electrons will transfer from Bi_2MoO_6 to MWCNTs until the equilibrium of Fermi levels, therefore, the heterojunctions will be formed at the interface after the Bi_2MoO_6 is compounded with MWCNTs. The energy band diagram of MWCNTs/Bi_2MoO_6 (Fig. 8b) depicts the electrons migrate to the MWCNTs from the conduction band of Bi_2MoO_6, while the holes will move in the opposite direction of the electrons. A larger carrier depletion region and potential barrier height will be formed, leading to a high baseline resistance. Moreover, the energy band structure of the pure Bi_2MoO_6 and MWCNTs/Bi_2MoO_6 heterojunction in a whole response-recovery process is displayed in Fig. S13. The more significant shrink of carrier depletion region and potential barrier height (ΔV_b) will occur in 2-CBMO once NH_3 is injected. Based on the equation ($\Delta R \propto \exp\{-q\Delta V_b/k_BT\}$, where ΔR is the variation of resistance, ΔV_b is the decrease of the potential barrier height, T and k_B represent temperature and Boltzmann constant, respectively.) [57], there will cause a sharp resistance decrease (ΔR) for 2-CBMO because of the large variation of potential barrier height, which will contribute to attaining superior sensing sensitivity.

The n-type semiconductor response (R_a/R_g) can be rewritten as $\sigma_g/\sigma_a = (c_g e\mu_p)/(c_a e\mu_p)$ (σ_a and σ_g, conductivity in air and gas; c_a and c_g, electrons concentrations in air and gas; e, charge, μ_p, electron mobility) [58]. The electron mobilities of a sensor in different gas can be defined as the same. Then, the equation can be transformed into the following:

$$S = \frac{R_a}{R_g} = \frac{c_g}{c_a} = \frac{c_a + (c_g\text{-}c_a)}{c_a} = \frac{\Delta c}{c_a} + 1 \quad (6)$$

where $\Delta c = c_g\text{-}c_a$ represents the change of electrons concentrations. Based on the above three points, the 2-CBMO composites sensor will possess the lower c_a in air and larger Δc in the response/recovery process, which means a higher response can be attained. Furthermore, the experimental details in Fig. S14 clarify the above two aspects. 2-CBMO shows a higher baseline resistance (R_a, 7.85×10^{10} Ω) and a larger resistance variation (ΔR, 7.68×10^{10} Ω), while that of BMO is 4.32×10^9 Ω and 4.01×10^9 Ω, respectively. The experimental details further confirm the lower c_a and larger Δc of 2-CBMO, indicating that the advanced 2-CBMO composites gas sensor benefits from the MWCNTs compounding.

Additionally, the re-orientated facets growth of 2-CBMO contributes to improving surface activity for the oxidation of NH_3. Based on the observed results of HRTEM, the two different exposed facets of Bi_2MoO_6 are schematically illustrated in Fig. 9a and b. The alternating layered structure is favorable for electron conductivity, which can guarantee a fast response of sensor [40,59]. Moreover, according to the reported works, the {010} facets of Bi_2MoO_6 are in favor of promoting reaction kinetics and improving the gas-solid phase reaction [19,60]. To theoretically illustrate the enhanced effect of the induced facets, the adsorption conformations and energies of NH_3 on (002) and (060) facets of Bi_2MoO_6 were studied using DFT calculations. As shown in Fig. 9c and d, the nearest distance between NH_3 molecule and the substrates are 2.607 Å and 2.287 Å, while the NH_3 adsorption energies on the surface are − 0.37 eV and − 0.87 eV, respectively. The cleaved (060) crystal planes of Bi_2MoO_6 showed the lower NH_3 adsorption energy, indicating that compounding MWCNTs is advantageous for NH_3 adsorption, electrons transfer and attaining superior sensing properties.

4. Conclusions

In this work, we synthesized pure Bi_2MoO_6 nanosheets and MWCNTs/Bi_2MoO_6 composites based NH_3 gas sensors using a simple hydrothermal synthesis route. The effect of MWCNTs and {010} crystal facets of Bi_2MoO_6 on the nanostructure and sensing properties of Bi_2MoO_6 based gas sensors were investigated systematically. Among them, the 0.5 wt% MWCNTs/Bi_2MoO_6 (2-CBMO) exhibited the highest response to 10–50 ppm NH_3 and advanced response/recover speed, LOD (157 ppb), selectivity, humidity resistance and operating stability. Combining the multiple experimental and DFT simulation results, the synergistic effect of 1D/2D nanostructure, inducing growth of high-energy facet and p-n heterojunctions was used to explain the achieved superior gas sensing performance at room temperature. This work is expected to develop high-performance room temperature NH_3 sensors for practical application.

CRediT authorship contribution statement

Kaidi Wu: Conceptualization, Methodology, Investigation, Formal analysis, Writing – original draft. **Hongfeng Chai:** Investigation, Writing – review & editing. **Kaichun Xu:** Investigation, Writing – review & editing. **Marc Debliquy:** Formal analysis, Writing – review & editing, Resources, Supervision. **Chao Zhang:** Conceptualization, Writing – review & editing, Supervision, Funding acquisition.

Declaration of Competing Interest

The authors declare that they have no known competing financial interests or personal relationships that could have appeared to influence the work reported in this paper.

Data availability

Data will be made available on request.

Acknowledgment

This work is supported by the Outstanding Youth Foundation of Jiangsu Province of China under Grant No. BK20211548, the Natural Science Foundation of China under Grant No. 51872254, the Postgraduate Research & Practice Innovation Program of Jiangsu Province under Grant No. KYCX21_3229 and the Excellent Doctoral Dissertation Fund of Yangzhou University (2021_06).

Appendix A. Supporting information

Supplementary data associated with this article can be found in the online version at doi:10.1016/j.snb.2022.132983.

References

[1] M.A.A. Mamun, M.R. Yuce, Recent progress in nanomaterial enabled chemical sensors for wearable environmental monitoring applications, Adv. Funct. Mater. 30 (2020), 2005703, https://doi.org/10.1002/adfm.202005703.
[2] D.W. Kang, S.E. Ju, D.W. Kim, M. Kang, H. Kim, C.S. Hong, Emerging porous materials and their composites for NH_3 gas removal, Adv. Sci. 7 (2020), 2002142, https://doi.org/10.1002/advs.202002142.
[3] N. Tang, C. Zhou, L. Xu, Y. Jiang, H. Qu, X. Duan, A fully integrated wireless flexible ammonia sensor fabricated by soft nano-lithography, ACS Sens 4 (2019) 726–732, https://doi.org/10.1021/acssensors.8b01690.
[4] K. Wu, M. Debliquy, C. Zhang, Room temperature gas sensors based on Ce doped TiO_2 nanocrystals for highly sensitive NH_3 detection, Chem. Eng. J. 444 (2022), 136449, https://doi.org/10.1016/j.cej.2022.136449.
[5] H.-Y. Li, C.-S. Lee, D.H. Kim, J.-H. Lee, Flexible room-temperature NH_3 Sensor for ultrasensitive, selective, and humidity-independent gas detection, ACS Appl. Mater. Interfaces 10 (2018) 27858–27867, https://doi.org/10.1021/acsami.8b09169.
[6] D. Kwak, Y. Lei, R. Maric, Ammonia gas sensors: A comprehensive review, Talanta 204 (2019) 713–730, https://doi.org/10.1016/j.talanta.2019.06.034.
[7] K. Shingange, Z.P. Tshabalala, O.M. Ntwaeaborwa, D.E. Motaung, G.H. Mhlongo, Highly selective NH_3 gas sensor based on Au loaded ZnO nanostructures prepared using microwave-assisted method, J. Colloid Interface Sci. 479 (2016) 127–138, https://doi.org/10.1016/j.jcis.2016.06.046.
[8] Y. Xiong, Z. Zhu, T. Guo, H. Li, Q. Xue, Synthesis of nanowire bundle-like WO_3-$W_{18}O_{49}$ heterostructures for highly sensitive NH_3 sensor application, J. Hazard. Mater. 353 (2018) 290–299, https://doi.org/10.1016/j.jhazmat.2018.04.020.
[9] Q. Qi, P.-P. Wang, J. Zhao, L.-L. Feng, L.-J. Zhou, R.-F. Xuan, Y.-P. Liu, G.-D. Li, SnO_2 nanoparticle-coated In_2O_3 nanofibers with improved NH_3 sensing properties, Sens. Actuators B Chem. 194 (2014) 440–446, https://doi.org/10.1016/j.snb.2013.12.115.

[10] J. Sun, Y. Wang, P. Song, Z. Yang, Q. Wang, Metal-organic framework-derived Cr-doped hollow In_2O_3 nanoboxes with excellent gas-sensing performance toward ammonia, J. Alloy. Compd. 879 (2021), 160472, https://doi.org/10.1016/j.jallcom.2021.160472.

[11] Y. Zhou, Y. Wang, Y. Wang, H. Yu, R. Zhang, J. Li, Z. Zang, X. Li, MXene $Ti_3C_2T_x$-derived nitrogen-functionalized heterophase TiO_2 homojunctions for room-temperature trace ammonia gas sensing, ACS Appl. Mater. Interfaces 13 (2021) 56485–56497, https://doi.org/10.1021/acsami.1c17429.

[12] B. Wu, L. Wang, H. Wu, K. Kan, G. Zhang, Y. Xie, Y. Tian, L. Li, K. Shi, Templated synthesis of 3D hierarchical porous Co_3O_4 materials and their NH_3 sensor at room temperature, Microporous Mesoporous Mater. 225 (2016) 154–163, https://doi.org/10.1016/j.micromeso.2015.12.019.

[13] K.-D. Wu, J.-Y. Xu, M. Debliquy, C. Zhang, Synthesis and NH_3/TMA sensing properties of $CuFe_2O_4$ hollow microspheres at low working temperature, Rare Met 40 (2021) 1768–1777, https://doi.org/10.1007/s12598-020-01609-9.

[14] Diversiform metal oxide-based hybrid nanostructures for gas sensing with versatile prospects, in: D. Zhang, Z. Yang, S. Yu, Q. Mi, Q. Pan (Eds.), Coord. Chem. Rev., 413, 2020, https://doi.org/10.1016/j.ccr.2020.213272.

[15] S. Das, S. Mojumder, D. Saha, M. Pal, Influence of major parameters on the sensing mechanism of semiconductor metal oxide based chemiresistive gas sensors: A review focused on personalized healthcare, Sens. Actuators B Chem. 352 (2022), 131066, https://doi.org/10.1016/j.snb.2021.131066.

[16] L. Siebert, N. Wolff, N. Ababii, M.-I. Terasa, O. Lupan, A. Vahl, V. Duppel, H. Qiu, M. Tienken, M. Mirabelli, V. Sontea, F. Faupel, L. Kienle, R. Adelung, Facile fabrication of semiconducting oxide nanostructures by direct ink writing of readily available metal microparticles and their application as low power acetone gas sensors, Nano Energy 70 (2020), 104420, https://doi.org/10.1016/j.nanoen.2019.104420.

[17] H. Li, W. Li, S. Gu, F. Wang, X. Liu, C. Ren, Forming oxygen vacancies inside in lutetium-doped Bi_2MoO_6 nanosheets for enhanced visible-light photocatalytic activity, Mol. Catal. 433 (2017) 301–312, https://doi.org/10.1016/j.mcat.2017.02.042.

[18] Z. Yang, M. Shen, K. Dai, X. Zhang, H. Chen, Controllable synthesis of Bi_2MoO_6 nanosheets and their facet-dependent visible-light-driven photocatalytic activity, Appl. Surf. Sci. 430 (2018) 505–514, https://doi.org/10.1016/j.apsusc.2017.08.072.

[19] G. Yang, Y.-A. Zhu, Y. Liang, J. Yang, K. Wang, Z. Zeng, R. Xu, X. Xie, Crystal defect-mediated {010} facets of Bi_2MoO_6 nanosheets for removal of TC: Enhanced mechanism and degradation pathway, Appl. Surf. Sci. 539 (2021), 148038, https://doi.org/10.1016/j.apsusc.2020.148038.

[20] H. Ma, Y. He, X. Li, J. Sheng, J. Li, F. Dong, Y. Sun, In situ loading of MoO_3 clusters on ultrathin Bi_2MoO_6 nanosheets for synergistically enhanced photocatalytic NO abatement, Appl. Catal. B Environ. 292 (2021), 120159, https://doi.org/10.1016/j.apcatb.2021.120159.

[21] Y. Qin, S. Liu, X. Shen, H. Gui, Y. Bai, Enhanced gas sensing performance of Bi_2MoO_6 with introduction of oxygen vacancy: Coupling of experiments and first-principles calculations, J. Alloy. Compd. 894 (2022), 162534, https://doi.org/10.1016/j.jallcom.2021.162534.

[22] A.G. Bannov, O. Jašek, A. Manakhov, M. Márik, D. Nečas, L. Zajíčková, High-performance ammonia gas sensors based on plasma treated carbon nanostructures, IEEE Sens. J. 17 (2017) 1964–1970, https://doi.org/10.1109/JSEN.2017.2656122.

[23] L.A. Panes-Ruiz, M. Shaygan, Y. Fu, Y. Liu, V. Khavrus, S. Oswald, T. Gemming, L. Baraban, V. Bezugly, G. Cuniberti, Toward highly sensitive and energy efficient ammonia gas detection with modified single-walled carbon nanotubes at room temperature, ACS Sens 3 (2018) 79–86, https://doi.org/10.1021/acssensors.7b00358.

[24] M. Yang, C. Au, G. Deng, S. Mathur, Q. Huang, X. Luo, G. Xie, H. Tai, Y. Jiang, C. Chen, Z. Cui, X. Liu, C. He, Y. Su, J. Chen, $NiWO_4$ microflowers on multi-walled carbon nanotubes for high-performance NH_3 detection, ACS Appl. Mater. Interfaces 13 (2021) 52850–52860, https://doi.org/10.1021/acsami.1c10805.

[25] F. Hosseini, A. Kasaeian, F. Pourfayaz, M. Sheikhpour, D. Wen, Novel ZnO-Ag/MWCNT nanocomposite for the photocatalytic degradation of phenol, Mater. Sci. Semicond. Process. 83 (2018) 175–185, https://doi.org/10.1016/j.mssp.2018.04.042.

[26] I. Ahmad, S. Shukrullah, M.Y. Naz, E. Ahmed, M. Ahmad, Rare earth metals co-doped ZnO/CNTs composite as high performance photocatalyst for hydrogen production from water_triethanolmine mixture, Int. J. Hydrog. Energy 47 (2022) 9283–9294, https://doi.org/10.1016/j.ijhydene.2022.01.006.

[27] R. Gang, L. Xu, Y. Xia, J. Cai, L. Zhang, S. Wang, R. Li, Fabrication of MoS_2 QDs/ZnO nanosheet 0D/2D heterojunction photocatalysts for organic dyes and gaseous heavy metal removal, J. Colloid Interface Sci. 579 (2020) 853–861, https://doi.org/10.1016/j.jcis.2020.06.116.

[28] W. Wang, W. Dong, X. Hong, Y. Liu, S. Yang, Preparation of g-C_3N_4/CNTs composite by dissolution-precipitation method as sulfur host for high-performance lithium-sulfur batteries, Mater. Chem. Phys. 283 (2022), 126014, https://doi.org/10.1016/j.matchemphys.2022.126014.

[29] J. Long, S. Wang, H. Chang, B. Zhao, B. Liu, Y. Zhou, W. Wei, X. Wang, L. Huang, W. Huang, Bi_2MoO_6 nanobelts for crystal facet-enhanced photocatalysis, Small 10 (2014) 2791–2795, https://doi.org/10.1002/smll.201302950.

[30] S. Wang, X. Ding, N. Yang, G. Zhan, X. Zhang, G. Dong, L. Zhang, H. Chen, Insight into the effect of bromine on facet-dependent surface oxygen vacancies construction and stabilization of Bi_2MoO_6 for efficient photocatalytic NO removal, Appl. Catal. B Environ. 265 (2020), 118585, https://doi.org/10.1016/j.apcatb.2019.118585.

[31] N.M. Hung, N.D. Chinh, T.D. Nguyen, E.T. Kim, G. Choi, C. Kim, D. Kim, Carbon nanotube-metal oxide nanocomposite gas sensing mechanism assessed via NO_2 adsorption on n-WO_3/p-MWCNT nanocomposites, Ceram. Int. 46 (2020) 29233–29243, https://doi.org/10.1016/j.ceramint.2020.08.097.

[32] J.H. Lehman, M. Terrones, E. Mansfield, K.E. Hurst, V. Meunier, Evaluating the characteristics of multiwall carbon nanotubes, Carbon 49 (2011) 2581–2602, https://doi.org/10.1016/j.carbon.2011.03.028.

[33] Gh Eshaq, A. M, M.A. Khan, Z.A. Alothman, M. Sillanpää, A novel Sm doped Cr_2O_3 sesquioxide-decorated MWCNTs heterostructured Fenton-like with sonophotocatalytic activities under visible light irradiation, J. Hazard. Mater. 426 (2022), 127812, https://doi.org/10.1016/j.jhazmat.2021.127812.

[34] S. Wang, X. Yang, X. Zhang, X. Ding, Z. Yang, K. Dai, H. Chen, A plate-on-plate sandwiched Z-scheme heterojunction photocatalyst: BiOBr-Bi_2MoO_6 with enhanced photocatalytic performance, Appl. Surf. Sci. 391 (2017) 194–201, https://doi.org/10.1016/j.apsusc.2016.07.070.

[35] Y. Qin, S. Liu, X. Shen, H. Gui, Y. Bai, Enhanced gas sensing performance of Bi_2MoO_6 with introduction of oxygen vacancy: Coupling of experiments and first-principles calculations, J. Alloy. Compd. 894 (2022), 162534, https://doi.org/10.1016/j.jallcom.2021.162534.

[36] H. Lan, J. Zhou, Z. Hou, X. An, H. Liu, J. Qu, Defect modulation of MOF-derived $ZnFe_2O_4$/CNTs microcages for persulfate activation: Enhanced nonradical catalytic oxidation, Chem. Eng. J. 431 (2022), 133369, https://doi.org/10.1016/j.cej.2021.133369.

[37] J. Zhao, J. Zhang, L. Wang, J. Li, T. Feng, J. Fan, L. Chen, J. Gu, Superior wave-absorbing performances of silicone rubber composites via introducing covalently bonded SnO_2@MWCNT absorbent with encapsulation structure, Compos. Commun. 22 (2020), 100486, https://doi.org/10.1016/j.coco.2020.100486.

[38] C. Ma, W. Zhang, Y.-S. He, Q. Gong, H. Che, Z.-F. Ma, Carbon coated SnO_2 nanoparticles anchored on CNT as a superior anode material for lithium-ion batteries, Nanoscale 8 (2016) 4121–4126, https://doi.org/10.1039/C5NR07996A.

[39] J.-M. Wu, Y. Chen, L. Pan, P. Wang, Y. Cui, D. Kong, L. Wang, X. Zhang, J.-J. Zou, Multi-layer monoclinic $BiVO_4$ with oxygen vacancies and V^{4+} species for highly efficient visible-light photoelectrochemical applications, Appl. Catal. B Environ. 221 (2018) 187–195, https://doi.org/10.1016/j.apcatb.2017.09.031.

[40] H. Li, J. Liu, W. Hou, N. Du, R. Zhang, X. Tao, Synthesis and characterization of g-C_3N_4/ Bi_2MoO_6 heterojunctions with enhanced visible light photocatalytic activity, Appl. Catal. B Environ. 160–161 (2014) 89–97, https://doi.org/10.1016/j.apcatb.2014.05.019.

[41] C. Zhang, K. Wu, H. Liao, M. Debliquy, Room temperature WO_3-Bi_2WO_6 sensors based on hierarchical microflowers for ppb-level H_2S detection, Chem. Eng. J. 430 (2022), 132813, https://doi.org/10.1016/j.cej.2021.132813.

[42] W.M. Taha, M. Morsy, N.A. Nada, M. Ibrahim, Studying the humidity sensing behavior of MWCNTs boosted with Co_3O_4 nanorods, Diam. Relat. Mater. 121 (2022), 108754, https://doi.org/10.1016/j.diamond.2021.108754.

[43] M.D. Fernández-Ramos, L.F. Capitán-Vallvey, L.M. Pastrana-Martínez, S. Morales-Torres, F.J. Maldonado-Hódar, Chemoresistive NH_3 gas sensor at room temperature based on the carbon gel-TiO_2 nanocomposites, Sens. Actuators B Chem. (2022), 132103, https://doi.org/10.1016/j.snb.2022.132103.

[44] S.X. Fan, W. Tang, Synthesis, characterization and mechanism of electrospun carbon nanofibers decorated with ZnO nanoparticles for flexible ammonia gas sensors at room temperature, Sens. Actuators B Chem. 362 (2022), 131789, https://doi.org/10.1016/j.snb.2022.131789.

[45] J. Huang, D. Jiang, J. Zhou, J. Ye, Y. Sun, X. Li, Y. Geng, J. Wang, Y. Du, Z. Qian, Visible light-activated room temperature NH_3 sensor base on CuPc-loaded ZnO nanorods, Sens. Actuators B Chem. 327 (2021) 128911, https://doi.org/10.1016/j.snb.2020.128911.

[46] A. Liu, S. Lv, L. Zhao, F. Liu, J. Wang, R. You, Z. Yang, J. He, L. Jiang, C. Wang, X. Yan, P. Sun, G. Lu, Room temperature flexible NH_3 sensor based on polyaniline coated Rh-doped SnO_2 hollow nanotubes, Sens. Actuators B Chem. 330 (2021) 129313, https://doi.org/10.1016/j.snb.2020.129313.

[47] P. Li, B. Wang, C. Qin, C. Han, L. Sun, Y. Wang, Band-gap-tunable CeO_2 nanoparticles for room-temperature NH_3 gas sensors, Ceram. Int. 46 (2020) 19232–19240, https://doi.org/10.1016/j.ceramint.2020.04.261.

[48] S. Kumar, A. Singh, R. Singh, S. Singh, P. Kumar, R. Kumar, Facile h-MoO_3 synthesis for NH_3 gas sensing application at moderate operating temperature, Sens. Actuators B Chem. 325 (2020) 128974, https://doi.org/10.1016/j.snb.2020.128974.

[49] H. Tai, Z. Duan, Z. He, X. Li, J. Xu, B. Liu, Y. Jiang, Enhanced ammonia response of $Ti_3C_2T_x$ nanosheets supported by TiO_2 nanoparticles at room temperature, Sens. Actuators B Chem. 298 (2019) 126874, https://doi.org/10.1016/j.snb.2019.126874.

[50] L. Vatandoust, A. Habibi, H. Naghshara, S.M. Aref, Fabrication of ZnO-MWCNT nanocomposite sensor and investigation of its ammonia gas sensing properties at room temperature, Synth. Met. 273 (2021) 116710, https://doi.org/10.1016/j.synthmet.2021.116710.

[51] Y. Tu, C. Kyle, H. Luo, D.-W. Zhang, A. Das, J. Briscoe, S. Dunn, M.-M. Titirici, S. Krause, Ammonia gas sensor response of a vertical zinc oxide nanorod-gold junction diode at room temperature, ACS Sens 5 (2020) 3568–3575, https://doi.org/10.1021/acssensors.0c01769.

[52] X. Dong, X. Cheng, X. Zhang, L. Sui, Y. Xu, S. Gao, H. Zhao, L. Huo, A novel coral-shaped Dy_2O_3 gas sensor for high sensitivity NH_3 detection at room temperature, Sens. Actuators B Chem. 255 (2018) 1308–1315, https://doi.org/10.1016/j.snb.2017.08.117.

[53] J. Wang, Z. Li, S. Zhang, S. Yan, B. Cao, Z. Wang, Y. Fu, Enhanced NH_3 gas-sensing performance of silica modified CeO_2 nanostructure based sensors, Sens. Actuators B Chem. 255 (2018) 862–870, https://doi.org/10.1016/j.snb.2017.08.149.

[54] M.-H. Kim, J.-S. Jang, W.-T. Koo, S.-J. Choi, S.-J. Kim, D.-H. Kim, I.-D. Kim, Bimodally porous WO_3 microbelts functionalized with Pt catalysts for selective H_2S sensors, ACS Appl. Mater. Interfaces 10 (2018) 20643–20651, https://doi.org/10.1021/acsami.8b00588.
[55] W. Huo, W. Xu, T. Cao, Z. Guo, X. Liu, G. Ge, N. Li, T. Lan, H.-C. Yao, Y. Zhang, F. Dong, Carbonate doped Bi_2MoO_6 hierarchical nanostructure with enhanced transformation of active radicals for efficient photocatalytic removal of NO, J. Colloid Interface Sci. 557 (2019) 816–824, https://doi.org/10.1016/j.jcis.2019.09.089.
[56] T. Wang, P. Sun, F. Liu, G. Lu, Revealing the correlation between gas selectivity and semiconductor energy band structure derived from off-stoichiometric spinel $CdGa_2O_4$, Sens. Actuators B Chem. 352 (2022), 131039, https://doi.org/10.1016/j.snb.2021.131039.
[57] X. Hou, Y. Gao, H. Ji, S. Yi, Z. Zhang, T. Li, Y. Wang, L. Yuan, R. Zhang, J. Sun, D. Chen, Enhanced triethylamine-sensing properties of hierarchical molybdenum trioxide nanostructures derived by oxidizing molybdenum disulfide nanosheets, J. Colloid Interface Sci. 605 (2022) 624–636, https://doi.org/10.1016/j.jcis.2021.07.053.
[58] H.-J. Kim, K.-I. Choi, K.-M. Kim, C.W. Na, J.-H. Lee, Highly sensitive C_2H_5OH sensors using Fe-doped NiO hollow spheres, Sens. Actuators B Chem. 171–172 (2012) 1029–1037, https://doi.org/10.1016/j.snb.2012.06.029.
[59] G. Yang, Y. Liang, K. Li, J. Yang, R. Xu, X. Xie, Construction of a Ce^{3+} doped CeO_2/Bi_2MoO_6 heterojunction with a mutual component activation system for highly enhancing the visible-light photocatalytic activity for removal of TC or Cr(VI), Inorg. Chem. Front. 6 (2019) 1507–1517, https://doi.org/10.1039/C9QI00302A.
[60] Y. Zheng, T. Zhou, X. Zhao, W.K. Pang, H. Gao, S. Li, Z. Zhou, H. Liu, Z. Guo, Atomic interface engineering and electric-field effect in ultrathin Bi_2MoO_6 nanosheets for superior lithium ion storage, Adv. Mater. 29 (2017), 1700396, https://doi.org/10.1002/adma.201700396.

Kaidi Wu received his B.S. degree in 2017 at Anhui University of Science and Technology (China). He is currently pursuing his joint Ph.D degree at Yangzhou University and University of Mons. He takes interests in smart materials for high-performance gas sensors working at room temperature.

Hongfeng Chai received his B.S. degree in 2020 at Yangzhou University (China). He is currently pursuing his Master degree at Yangzhou University. He takes interests in metal oxides based gas sensors for detecting VOCs.

Kaichun Xu received his B.S. degree in 2021 at Yangzhou University (China). He is currently pursuing his Master degree at Yangzhou University. He takes interests in high-performance metal oxides based gas sensors.

Marc Debliquy received his Ph.D. at Faculty of Engineering in Mons (Belgium) in1999 in the field of organic semiconductors for fire detection. He joined the Sochinor Company in 2000. He left in 2003 for joining Materia Nova. He was responsible for the research activities in the field of gas sensors. Since October 2008, he joined the Material Science Department of Faculty of Engineering of University of Mons and worked as a team leader of semiconductor and sensor group. He was promoted as associate professor in September 2013. His main research interest is smart coatings for chemical detection. He is also co-founder of the spin off company B-Sens specialized in optical fiber sensors.

Chao Zhang received a B.S. degree from the Chongqing University (China) in 2003 and a joint Ph.D. degree from Technology University of Belfort-Montbéliard (France) and Xi'an Jiaotong University (China) in June 2008. From September 2007 to January 2009, he worked as a teaching-research assistant in Technology University of Belfort-Montbéliard. Since Feb 2009, he is postdoctoral researcher, and then a senior researcher in Materials Science Department of engineering School of University of Mons (Belgium). In 2014, he joined Yangzhou University China) as professor where he is leading a research group on thermal spray coatings and gas sensors. Since August 2016, he is Vice Dean in charge of research in College of Mechanical Engineering. His research interests include thermal-sprayed techniques and coatings, especially gas sensing and wear-resistant coatings.